B_K with two flavors of dynamical overlap fermions

S. Aoki,[1,2] H. Fukaya,[3] S. Hashimoto,[4,5] J. Noaki,[4] T. Kaneko,[4,5] H. Matsufuru,[4] T. Onogi,[6] and N. Yamada[4,5]

(JLQCD Collaboration)

[1]*Graduate School of Pure and Applied Sciences, University of Tsukuba, Tsukuba 305-8571, Japan*
[2]*Riken BNL Research Center, Brookhaven National Laboratory, Upton, New York 11973, USA*
[3]*The Niels Bohr Institute, The Niels Bohr International Academy, Blegdamsvej 17 DK-2100 Copenhagen Ø, Denmark*
[4]*High Energy Accelerator Research Organization (KEK), Tsukuba 305-0801, Japan*
[5]*School of High Energy Accelerator Science, The Graduate University for Advanced Studies (Sokendai), Tsukuba 305-0801, Japan*
[6]*Yukawa Institute for Theoretical Physics, Kyoto University, Kyoto 606-8502, Japan*

We present a two-flavor QCD calculation of B_K on a $16^3 \times 32$ lattice at $a \sim 0.12$ fm (or equivalently $a^{-1} = 1.67$ GeV). Both valence and sea quarks are described by the overlap fermion formulation. The matching factor is calculated nonperturbatively with the so-called RI/MOM scheme. We find that the lattice data are well described by the next-to-leading order (NLO) partially quenched chiral perturbation theory (PQChPT) up to around a half of the strange quark mass ($m_s^{\text{phys}}/2$). The data at quark masses heavier than $m_s^{\text{phys}}/2$ are fitted including a part of next-to-next-to-leading order terms. We obtain $B_K^{\overline{\text{MS}}}(2 \text{ GeV}) = 0.537(4)(40)$, where the first error is statistical and the second is an estimate of systematic uncertainties from finite volume, fixing topology, the matching factor, and the scale setting.

I. INTRODUCTION

The indirect CP violation in neutral kaon decays, characterized by the $|\epsilon_K|$ parameter, plays an important role to constrain the Cabibbo-Kobayashi-Maskawa (CKM) matrix elements. Experimentally, $|\epsilon_K|$ has been measured to an excellent precision, $|\epsilon_K| = (2.233 \pm 0.015) \times 10^{-3}$ [1], through the two pion decays of long-lived neutral kaons. Within the standard model, $|\epsilon_K|$ is expressed as [2]

$$|\epsilon_K| = (\text{known factor}) \times B_K(\mu) \times f(\bar{\rho}, \bar{\eta}), \quad (1)$$

where $f(\bar{\rho}, \bar{\eta})$ is a known function of the Wolfenstein parameters, $\bar{\rho}$ and $\bar{\eta}$, and $B_K(\mu)$ is a less known hadronic matrix element defined by

$$B_K(\mu) = \frac{\langle \bar{K}^0 | \bar{d}\gamma_\mu(1 - \gamma_5)s\bar{d}\gamma_\mu(1 - \gamma_5)s | K^0 \rangle}{\frac{8}{3}f_K^2 m_K^2}. \quad (2)$$

The $\Delta S = 2$ four-quark operator $\bar{d}\gamma_\mu(1 - \gamma_5)s\bar{d}\gamma_\mu(1 - \gamma_5)s$ is renormalized at a scale μ. The parameters appearing in the denominator, f_K and m_K, denote the leptonic decay constant and mass of kaon, respectively. Since the precision of the constraint on the fundamental parameters such as $(\bar{\rho}, \bar{\eta})$ is limited by the theoretical uncertainty in the kaon B parameter B_K, its precise calculation has a direct relevance to the study of the flavor structure of the standard model and beyond. The purpose of this study is to provide such a precise calculation of B_K using lattice QCD.

The numerator in (2) involving the $(V - A) \times (V - A)$ four-quark operator behaves as m_K^2 for the external states at rest, hence it vanishes in the chiral limit of kaon. This

behavior is altered if the four-quark operator mixes with other operators with different chiral structures under renormalization. Since the denominator in (2) contains m_K^2 and so vanishes in the chiral limit too, the appearance of operators with different chirality in the numerator causes unphysical divergence in the ratio toward the chiral limit. In the lattice calculation with the Wilson-type fermion formulations, this problem occurs because the formulations explicitly violate the chiral symmetry. Calculation of B_K using the Wilson-type fermions, therefore, is not very precise due to the uncontrolled operator mixing (for recent efforts in unquenched calculations, see [3,4]). For this reason, the lattice calculation of B_K has historically been done using the staggered fermion formulation, with which the chiral symmetry is realized at a cost of introducing unwanted flavors. A quenched calculation using the staggered fermion [5] has long been a "benchmark" calculation until recently, which is $B_K(2 \text{ GeV}) = 0.628(42)$ without an estimate of quenching uncertainty. More recently, the domain-wall fermion, which respects an approximate chiral symmetry on the lattice without introducing extra flavors, is applied to the calculation of B_K. Quenched calculations showed that the lattice artifact is significantly smaller than that of the staggered fermion and hence the continuum extrapolation is more straightforward [6–8]. Therefore, a great effort has been made to realize unquenched simulations using the domain-wall fermion; a $2 + 1$-flavor calculation result has recently been presented by the RBC-UKQCD collaboration [9], which is $B_K(2 \text{ GeV}) = 0.524(10)(28)$ with a combined statistical (the first error) and systematic (the second) error being

6%. (An earlier result of two-flavor QCD is also available [10].)

This work improves these lattice calculations of B_K in several directions. First of all, we use the overlap fermion formulation, which exactly respects a lattice variant of chiral symmetry. The problem of the operator mixing is absent in this formulation. With the domain-wall fermion, this is a nontrivial problem, because there is a tiny but nonzero operator mixing which could be enhanced by the unsuppressed chiral behavior of wrong chirality operators as discussed above. A detailed study gives an estimate of order 0.1% effect for B_K [11], which is negligible in the precision we are aiming at, but a calculation without such a delicate problem from the beginning is desirable. The exact chiral symmetry also helps to further reduce the discretization effect, since the $O(a)$ effect is completely absent.

Second, the use of chiral perturbation theory (ChPT), and even partially quenched (PQ) ChPT is justified in the analysis of lattice data, especially in the chiral extrapolation. Because of the pion (and kaon) loop effect, B_K develops a nonanalytic quark mass dependence, the so-called chiral logarithm, which may give a non-negligible contribution in the chiral extrapolation of lattice data to the physical up and down quark masses. Whether the observed quark mass dependence of lattice data is well described by ChPT is a complicated problem, since the mass region where the ChPT formula is applicable is not known from the outset and thus has to be tested by the lattice calculation for each quantity of interest. This test is difficult without the exact chiral symmetry, because the ChPT formula itself must be modified by including the effect of the violated chiral symmetry. Another requirement for an unambiguous test is a sufficient number of data points. We explore a broader sea and valence quark mass region covered with significantly more data points than former studies. In this work, we perform the test using the next-to-leading order (NLO) PQChPT formula by varying the sea quark mass region in the fit. The statistical signal of individual data points is improved by accumulating more statistics and by using a new technique, i.e., low-mode averaging. As a consequence, we are able to identify the applicability region of the NLO PQChPT, which makes the chiral extrapolation more reliable.

In spite of these obvious advantages, the overlap fermion formulation has not been used extensively especially for dynamical fermion simulations. The main problem is in its large computational cost to approximate the matrix sign function appearing in the definition of the overlap operator. Superficially, the cost is similar to that of the domain-wall fermion which requires N_s (length in the fifth dimension) times more computation, but in the hybrid Monte Carlo (HMC) simulation, the overlap fermion is much harder because of the discontinuity of the sign function, which requires a special trick, such as the "reflection-refraction" [12]. This makes the dynamical overlap fermion simulation

substantially more costly. In this work, we avoid this problem by introducing a topology fixing term to a gauge field action [13], with which we never encounter the discontinuity of the sign function. The physical effect of fixing the topological charge can be understood and be estimated, at a solid theoretical ground, as a finite volume effect [14].

The overlap fermion simulation has already been applied to a calculation of pion and kaon masses and decay constants [15], pion form factor [16], $\pi^{\pm} - \pi^0$ mass splitting [17], topological susceptibility [18], and more applications are planned. The simulation is also extended to the ϵ-regime, where the sea quark mass is even smaller than the physical value, and is used to extract the chiral condensate and pion decay constant in the chiral limit [19–22]. An overview of our project is presented in [23].

A potential problem of our work is that the simulation is performed with two flavors of sea quarks that correspond to up and down quarks. The effect of the strange sea quark is neglected. Although we do not expect its significant effect on B_K, the actual correction is hardly estimated within the two-flavor theory. We therefore have a plan to extend this work to a $2 + 1$-flavor calculation [24], for which this work serves as a prototype calculation with an almost realistic setup.

The rest of this paper is organized as follows. The lattice actions and simulation parameters are described in Sec. II. The methods to calculate the bare B_K and the nonperturbative matching factor are introduced in Sec. III. In Sec. IV, we compare the quark mass dependence of B_K with the prediction of NLO PQChPT to see the consistency. In Sec. V, how to extract the physical B_K is presented. Systematic errors in our result are discussed in Sec. VI. A summary of this work is given in Sec. VII.

II. SIMULATION PARAMETERS

We perform the calculation on a $16^3 \times 32$ lattice using the Iwasaki gauge action. The periodic boundary condition is set in all four directions. Both dynamical and valence quarks are described by the overlap-Dirac operator [25,26],

$$D_{\rm ov}(m_q) = \left(m_0 + \frac{m_q}{2}\right) + \left(m_0 - \frac{m_q}{2}\right)\gamma_5 {\rm sgn}(H_W(-m_0)),$$

(3)

where m_q is a quark mass and $H_W(-m_0)$ denotes the standard Hermitian Wilson-Dirac operator with a negative mass. Throughout this work we take $m_0 = 1.6$. A generation of configurations with dynamical overlap quarks requires a huge computational cost. To accelerate HMC, we introduce extra (unphysical) Wilson fermion and ghost fields, which suppress the appearance of the zero mode of $H_W(-m_0)$ [13]. At a price, the global topological charge Q is frozen during the HMC evolution. At $\beta = 2.30$ the inverse lattice spacing is $1/a = 1.67(2)(2)$ GeV, which is determined through $r_0 = 0.49$ fm [27] in the $Q = 0$ sector.

The physical spatial volume of our lattice is about $(1.9 \text{ fm})^3$. We carry out the simulations at six sea quark masses: $m_{\text{sea}} = 0.015, 0.025, 0.035, 0.050, 0.070, 0.100$ in the lattice unit. These approximately cover the mass range $[m_s^{\text{phys}}/6, m_s^{\text{phys}}]$, where m_s^{phys} denotes the physical strange quark mass. The lightest pion is about 290 MeV, which gives $m_\pi L \sim 2.7$. The main calculation is made in the $Q = 0$ sector. In order to study the topological charge dependence, we have also generated configurations in the $Q = -2$ and -4 sectors at $m_{\text{sea}} = 0.050$. We have accumulated 10 000 trajectories for each sea quark mass at $Q = 0$ and 5000 at $Q = -2$ and -4. More details about the algorithm and parameters to generate the configurations are described in [28].

The calculation of B_K is done at every 20 trajectories for each sea quark mass, and a single jackknife bin consists of 5 measurements. For each sea quark mass, we take six valence quark masses and calculate B_K with all possible combinations of two valence quarks. The gauge is fixed to the Coulomb gauge except for the calculation of the nonperturbative matching factor, which is done in the Landau gauge. Low-mode averaging [29] is implemented for all correlation functions, which substantially improves the statistical signal.

III. METHOD AND RESULTS

A. Two-point functions and pseudoscalar meson masses

We calculate kaon two-point functions

$$C_{A_4A_4}^{(2),p-w}(t) = \sum_{\vec{x}} \langle A_4(t, \vec{x}) A_4^{\text{wall}}(0) \rangle, \quad (4)$$

with a wall source at t_{src} and a point sink at $t + t_{\text{src}}$. $A_4(t, \vec{x}) = \bar{q}_1(t, \vec{x}) \gamma_4 \gamma_5 q_2'(t, \vec{x})$ is the axial-vector current. The wall source is defined by $A_4^{\text{wall}}(t) = (\sum_{\vec{x}} \bar{q}_2(t, \vec{x})) \gamma_4 \gamma_5 \times (\sum_{\vec{y}} q_1(t, \vec{y}))$. q_1 and q_2 represent two different flavors of quarks described by the overlap formalism, and in the definition of the axial-vector current q_2 is modified to $q_2'(x) = [1 - D_{\text{ov}}(0)/(2m_0)] q_2(x)$ such that the axial-vector current exactly transforms into the vector current $V_4(t, \vec{x}) = \bar{q}_1(t, \vec{x}) \gamma_4 q_2'(t, \vec{x})$ under the axial transformation. We take an average of physically equivalent two-point functions over the four source points $t_{\text{src}} = 0, 8, 16, 24$. Because of the periodic boundary condition in the time direction, its asymptotic behavior in large t is given by

$$\text{eq.}(4) \rightarrow \frac{V_3 Z_{A_4}^{\text{wall}}}{2m_P} f_P m_P (e^{-m_P t} + e^{m_P(t-N_t)}), \quad (5)$$

where $N_t = 32$ and $V_3 = 16^3$. Data at two time slices equally separated from $t = 16$ are averaged. The correlated fit is carried out to extract m_P and $Z_{A_4}^{\text{wall}} f_P/2$, where

$$Z_{A_4}^{\text{wall}} = \langle P | \sum_{\vec{x}} \bar{q}_2(0, \vec{x}) \gamma_4 \gamma_5 q_1(0, \vec{0}) | 0 \rangle, \quad (6)$$

$$f_P m_P = \langle 0 | A_4(0) | P \rangle. \quad (7)$$

The fit range is chosen to be $t = [9, 16]$ for all the sea and valence quark masses. The numerical results for m_P and $Z_{A_4}^{\text{wall}} f_P/2$ are listed in Tables I, II, III, IV, V, VI, VII, and VIII for each ensemble. We also calculate pseudoscalar two-point functions $\langle PP \rangle$ and make a correlated fit to obtain the mass. Effective mass plots for the pseudoscalar and axial-vector two-point functions are compared in

TABLE I. Numerical results at $m_{\text{sea}} = 0.015$ in the $Q = 0$ sector.

m_{v1}	m_{v2}	m_P	$Z_{A_4}^{\text{wall}} f_P/2$	c_0	c_1	Δ_P	$B_P^{\overline{\text{MS}}}(2 \text{ GeV})$
0.015	0.015	0.172(1)	0.283(4)	0.106(4)	0.23(2)	0.02(1)	0.43(1)
0.025	0.015	0.197(1)	0.341(4)	0.164(5)	0.34(2)	0.02(1)	0.458(7)
0.025	0.025	0.220(1)	0.399(4)	0.235(6)	0.49(3)	0.019(9)	0.480(6)
0.035	0.015	0.220(1)	0.394(4)	0.228(6)	0.48(3)	0.02(1)	0.478(6)
0.035	0.025	0.240(1)	0.451(4)	0.311(7)	0.65(3)	0.021(8)	0.497(5)
0.035	0.035	0.259(1)	0.504(4)	0.400(8)	0.84(4)	0.022(8)	0.512(4)
0.050	0.015	0.250(1)	0.466(5)	0.334(8)	0.69(4)	0.021(9)	0.501(5)
0.050	0.025	0.268(1)	0.523(5)	0.435(8)	0.91(5)	0.023(8)	0.518(4)
0.050	0.035	0.285(1)	0.575(5)	0.540(9)	1.14(5)	0.024(7)	0.530(3)
0.050	0.050	0.3088(9)	0.649(5)	0.71(1)	1.50(6)	0.025(7)	0.545(3)
0.070	0.015	0.285(1)	0.553(5)	0.49(1)	1.02(6)	0.02(1)	0.525(4)
0.070	0.025	0.301(1)	0.610(5)	0.62(1)	1.29(6)	0.025(8)	0.539(3)
0.070	0.035	0.317(1)	0.663(5)	0.74(1)	1.56(7)	0.025(7)	0.549(3)
0.070	0.050	0.3384(9)	0.737(5)	0.94(1)	1.98(8)	0.025(7)	0.561(2)
0.070	0.070	0.3659(9)	0.829(5)	1.22(2)	2.6(1)	0.025(7)	0.575(2)
0.100	0.015	0.332(1)	0.668(7)	0.76(2)	1.6(1)	0.02(1)	0.552(4)
0.100	0.025	0.346(1)	0.727(6)	0.92(2)	1.9(1)	0.026(9)	0.564(3)
0.100	0.035	0.360(1)	0.780(6)	1.07(2)	2.2(1)	0.026(8)	0.572(3)
0.100	0.050	0.3792(9)	0.855(6)	1.31(2)	2.7(1)	0.025(7)	0.581(2)
0.100	0.070	0.4044(8)	0.948(6)	1.64(2)	3.4(1)	0.023(7)	0.593(2)
0.100	0.100	0.4403(8)	1.077(6)	2.17(3)	4.4(2)	0.020(8)	0.608(2)

TABLE II.   Numerical results at $m_{\text{sea}} = 0.025$ in the $Q = 0$ sector.

m_{v1}	m_{v2}	m_P	$Z_{A_4}^{\text{wall}} f_P/2$	c_0	c_1	Δ_P	$B_P^{\overline{\text{MS}}}(2 \text{ GeV})$
0.015	0.015	0.170(1)	0.314(4)	0.129(4)	0.28(2)	0.016(9)	0.43(1)
0.025	0.015	0.1963(9)	0.373(4)	0.194(5)	0.43(2)	0.023(8)	0.454(7)
0.025	0.025	0.2190(9)	0.430(4)	0.272(5)	0.60(3)	0.027(7)	0.477(5)
0.035	0.015	0.2189(9)	0.427(4)	0.265(6)	0.58(3)	0.028(8)	0.474(6)
0.035	0.025	0.2395(9)	0.482(4)	0.354(6)	0.78(4)	0.031(7)	0.494(4)
0.035	0.035	0.2585(8)	0.535(4)	0.447(7)	1.00(4)	0.033(7)	0.509(4)
0.050	0.015	0.2492(9)	0.500(4)	0.382(7)	0.85(4)	0.033(8)	0.496(5)
0.050	0.025	0.2675(9)	0.555(4)	0.486(7)	1.09(5)	0.034(7)	0.514(4)
0.050	0.035	0.2846(8)	0.606(4)	0.594(8)	1.34(6)	0.036(7)	0.527(3)
0.050	0.050	0.3087(8)	0.678(4)	0.766(9)	1.74(8)	0.037(7)	0.542(3)
0.070	0.015	0.2848(9)	0.589(5)	0.55(1)	1.25(7)	0.038(9)	0.519(4)
0.070	0.025	0.3010(9)	0.643(4)	0.68(1)	1.53(7)	0.037(7)	0.534(3)
0.070	0.035	0.3165(8)	0.693(4)	0.80(1)	1.83(8)	0.037(7)	0.545(3)
0.070	0.050	0.3384(8)	0.764(4)	1.00(1)	2.3(1)	0.038(7)	0.559(2)
0.070	0.070	0.3661(8)	0.854(4)	1.28(1)	2.9(1)	0.038(7)	0.573(2)
0.100	0.015	0.332(1)	0.708(6)	0.84(1)	1.9(1)	0.04(1)	0.545(4)
0.100	0.025	0.3461(9)	0.761(5)	0.99(1)	2.2(1)	0.038(8)	0.559(3)
0.100	0.035	0.3597(9)	0.811(5)	1.15(1)	2.6(1)	0.038(7)	0.568(2)
0.100	0.050	0.3795(8)	0.881(5)	1.38(2)	3.1(1)	0.038(7)	0.579(2)
0.100	0.070	0.4048(8)	0.971(5)	1.71(2)	3.9(2)	0.038(7)	0.591(2)
0.100	0.100	0.4408(8)	1.096(6)	2.24(3)	5.1(2)	0.038(7)	0.606(2)

Fig. 1. Horizontal lines show the mass and one-sigma band obtained from the fit, also indicating the fit ranges chosen. We confirm that the masses extracted from $\langle PP \rangle$ and $\langle A_4 A_4 \rangle$ are consistent within 1 standard deviation for all the cases. We use the mass from $\langle A_4 A_4 \rangle$ in the following analysis.

B. Three-point functions and B_P

In order to obtain B_K we also need to calculate three-point functions defined by

$$C_{L_\mu L_\mu}^{(3)}(t_2, t, t_1) = \sum_{\vec{x}} \langle A_4^{\text{wall}}(t_2) O_{L_\mu L_\mu}^{\text{lat}}(t, \vec{x}) A_4^{\text{wall}}(t_1) \rangle, \quad (8)$$

TABLE III.   Numerical results at $m_{\text{sea}} = 0.035$ in the $Q = 0$ sector.

m_{v1}	m_{v2}	m_P	$Z_{A_4}^{\text{wall}} f_P/2$	c_0	c_1	Δ_P	$B_P^{\overline{\text{MS}}}(2 \text{ GeV})$
0.015	0.015	0.173(1)	0.325(3)	0.138(5)	0.31(2)	0.02(1)	0.43(1)
0.025	0.015	0.199(1)	0.382(4)	0.203(5)	0.44(2)	0.019(9)	0.451(7)
0.025	0.025	0.2211(9)	0.437(4)	0.279(6)	0.60(3)	0.021(7)	0.474(6)
0.035	0.015	0.221(1)	0.436(4)	0.274(6)	0.59(3)	0.021(8)	0.470(6)
0.035	0.025	0.2416(9)	0.488(4)	0.360(7)	0.77(3)	0.023(7)	0.491(5)
0.035	0.035	0.2604(9)	0.538(4)	0.452(7)	0.98(4)	0.025(6)	0.507(4)
0.050	0.015	0.251(1)	0.509(4)	0.392(7)	0.84(4)	0.024(8)	0.492(5)
0.050	0.025	0.2695(9)	0.559(4)	0.491(8)	1.06(4)	0.025(6)	0.511(4)
0.050	0.035	0.2864(9)	0.608(4)	0.596(9)	1.29(5)	0.027(6)	0.525(4)
0.050	0.050	0.3104(8)	0.679(4)	0.77(1)	1.66(6)	0.028(6)	0.540(3)
0.070	0.015	0.287 (1)	0.599(5)	0.57(1)	1.20(6)	0.025(9)	0.514(4)
0.070	0.025	0.3030(9)	0.647(4)	0.68(1)	1.47(6)	0.027(7)	0.531(4)
0.070	0.035	0.3182(9)	0.694(4)	0.80(1)	1.74(7)	0.028(6)	0.543(3)
0.070	0.050	0.3401(8)	0.763(4)	1.00(1)	2.15(8)	0.028(6)	0.556(3)
0.070	0.070	0.3676(8)	0.852(5)	1.27(1)	2.7(1)	0.026(6)	0.571(3)
0.100	0.015	0.334(1)	0.719(6)	0.86(1)	1.8(1)	0.02(1)	0.538(4)
0.100	0.025	0.3479(9)	0.765(5)	1.00(1)	2.1(1)	0.026(7)	0.554(3)
0.100	0.035	0.3614(9)	0.811(5)	1.14(1)	2.4(1)	0.027(6)	0.564(3)
0.100	0.050	0.3810(8)	0.879(5)	1.37(2)	2.9(1)	0.026(6)	0.576(3)
0.100	0.070	0.4062(8)	0.967(5)	1.69(2)	3.5(1)	0.023(6)	0.589(3)
0.100	0.100	0.4422(8)	1.091(6)	2.21(2)	4.5(2)	0.018(7)	0.605(2)

TABLE IV. Numerical results at $m_{\text{sea}} = 0.050$ in the $Q = 0$ sector.

m_{v1}	m_{v2}	m_P	$Z_{A_4}^{\text{wall}} f_P/2$	c_0	c_1	Δ_P	$B_P^{\overline{\text{MS}}}(2 \text{ GeV})$
0.015	0.015	0.175(1)	0.350(3)	0.162(4)	0.34(2)	0.005(9)	0.430(8)
0.025	0.015	0.2006(9)	0.409(3)	0.236(5)	0.49(2)	0.011(8)	0.458(6)
0.025	0.025	0.2232(9)	0.464(3)	0.319(5)	0.67(3)	0.016(7)	0.481(5)
0.035	0.015	0.2234(9)	0.464(3)	0.317(6)	0.66(3)	0.016(8)	0.478(5)
0.035	0.025	0.2437(9)	0.515(3)	0.406(6)	0.86(4)	0.020(6)	0.498(4)
0.035	0.035	0.2626(9)	0.566(3)	0.504(7)	1.07(4)	0.023(6)	0.512(4)
0.050	0.015	0.2538(9)	0.540(4)	0.449(7)	0.95(5)	0.022(8)	0.501(4)
0.050	0.025	0.2718(9)	0.588(4)	0.549(8)	1.17(5)	0.024(6)	0.517(4)
0.050	0.035	0.2888(9)	0.635(4)	0.657(9)	1.41(6)	0.026(6)	0.529(3)
0.050	0.050	0.3128(9)	0.705(4)	0.83(1)	1.79(7)	0.028(6)	0.544(3)
0.070	0.015	0.290(1)	0.632(4)	0.64(1)	1.38(8)	0.027(9)	0.524(4)
0.070	0.025	0.3054(9)	0.677(4)	0.76(1)	1.63(7)	0.028(7)	0.537(3)
0.070	0.035	0.3207(9)	0.722(4)	0.88(1)	1.90(8)	0.029(6)	0.547(3)
0.070	0.050	0.3426(9)	0.789(4)	1.07(1)	2.33(9)	0.029(6)	0.560(3)
0.070	0.070	0.3703(8)	0.876(4)	1.36(2)	2.9(1)	0.030(6)	0.575(3)
0.100	0.015	0.337(1)	0.755(5)	0.96(2)	2.1(1)	0.03(1)	0.549(4)
0.100	0.025	0.351(1)	0.798(5)	1.10(1)	2.4(1)	0.032(8)	0.560(3)
0.100	0.035	0.3641(9)	0.841(5)	1.24(2)	2.7(1)	0.031(7)	0.569(3)
0.100	0.050	0.3838(9)	0.906(5)	1.47(2)	3.2(1)	0.031(7)	0.580(3)
0.100	0.070	0.4091(9)	0.991(5)	1.79(2)	3.9(2)	0.031(7)	0.593(3)
0.100	0.100	0.4452(9)	1.114(6)	2.32(3)	5.1(2)	0.032(7)	0.608(3)

where

$$O_{L_\mu L_\mu}^{\text{lat}} = \bar{q}_1 \gamma_\mu (1 - \gamma_5) q_2' \bar{q}_1 \gamma_\mu (1 - \gamma_5) q_2' \qquad (9)$$

is the $\Delta S = 2$ four-quark operator defined on the lattice. In the calculation of three-point functions, the kaon interpo-

lating operator, that is the wall source, is put at fixed time slices t_1 and t_2 while the position of four-quark operator t is varied as shown in Fig. 2. We take $|t_2 - t_1| = 16$ or 24, which we call set A and B, respectively. For set A we take $(t_2, t_1) = (16, 0)$ and $(24, 8)$, while for set B we take

TABLE V. Numerical results at $m_{\text{sea}} = 0.070$ in the $Q = 0$ sector.

m_{v1}	m_{v2}	m_P	$Z_{A_4}^{\text{wall}} f_P/2$	c_0	c_1	Δ_P	$B_P^{\overline{\text{MS}}}(2 \text{ GeV})$
0.015	0.015	0.1760(9)	0.365(4)	0.178(5)	0.34(2)	$-0.005(9)$	0.436(8)
0.025	0.015	0.2018(8)	0.423(4)	0.254(6)	0.49(3)	0.005(8)	0.462(6)
0.025	0.025	0.2243(8)	0.476(4)	0.338(6)	0.68(3)	0.013(7)	0.484(5)
0.035	0.015	0.2245(8)	0.477(4)	0.337(7)	0.67(3)	0.012(8)	0.481(5)
0.035	0.025	0.2448(8)	0.526(4)	0.426(7)	0.88(4)	0.020(7)	0.500(4)
0.035	0.035	0.2636(8)	0.575(4)	0.522(8)	1.11(5)	0.026(6)	0.514(4)
0.050	0.015	0.2547(8)	0.552(4)	0.472(9)	0.98(5)	0.021(8)	0.503(4)
0.050	0.025	0.2728(8)	0.597(4)	0.569(9)	1.22(5)	0.027(7)	0.519(4)
0.050	0.035	0.2898(7)	0.642(4)	0.67(1)	1.48(6)	0.032(6)	0.531(3)
0.050	0.050	0.3139(7)	0.710(4)	0.85(1)	1.90(8)	0.036(6)	0.546(3)
0.070	0.015	0.2903(8)	0.643(5)	0.67(1)	1.46(9)	0.031(9)	0.525(4)
0.070	0.025	0.3064(8)	0.684(4)	0.78(1)	1.72(8)	0.034(7)	0.539(3)
0.070	0.035	0.3217(7)	0.727(4)	0.89(1)	2.02(8)	0.037(6)	0.549(3)
0.070	0.050	0.3437(7)	0.793(4)	1.09(1)	2.5(1)	0.039(6)	0.562(2)
0.070	0.070	0.3714(7)	0.878(5)	1.36(2)	3.1(1)	0.039(6)	0.576(2)
0.100	0.015	0.3373(9)	0.766(6)	0.99(2)	2.3(2)	0.04(1)	0.551(4)
0.100	0.025	0.3514(8)	0.804(5)	1.12(2)	2.6(1)	0.043(8)	0.563(3)
0.100	0.035	0.3651(8)	0.845(5)	1.25(2)	2.9(1)	0.042(7)	0.571(3)
0.100	0.050	0.3849(7)	0.908(5)	1.47(2)	3.4(1)	0.041(6)	0.582(2)
0.100	0.070	0.4103(7)	0.991(5)	1.79(2)	4.1(2)	0.040(6)	0.594(2)
0.100	0.100	0.4464(7)	1.112(6)	2.32(2)	5.3(2)	0.039(6)	0.609(2)

TABLE VI. Numerical results at $m_{\text{sea}} = 0.100$ in the $Q = 0$ sector.

m_{v1}	m_{v2}	m_P	$Z_{A_4}^{\text{wall}} f_P/2$	c_0	c_1	Δ_P	$B_P^{\overline{\text{MS}}}(2\text{ GeV})$
0.015	0.015	0.1770(8)	0.374(3)	0.195(5)	0.42(3)	0.02(1)	0.454(8)
0.025	0.015	0.2032(8)	0.434(4)	0.276(5)	0.58(3)	0.018(8)	0.476(6)
0.025	0.025	0.2260(7)	0.490(3)	0.364(6)	0.75(3)	0.018(7)	0.494(4)
0.035	0.015	0.2261(8)	0.489(4)	0.362(6)	0.75(4)	0.020(7)	0.491(5)
0.035	0.025	0.2467(7)	0.541(4)	0.456(7)	0.94(4)	0.020(6)	0.507(4)
0.035	0.035	0.2657(7)	0.591(4)	0.557(8)	1.15(5)	0.021(6)	0.519(3)
0.050	0.015	0.2566(8)	0.565(4)	0.500(8)	1.05(5)	0.023(7)	0.509(4)
0.050	0.025	0.2749(7)	0.613(4)	0.604(8)	1.25(5)	0.022(6)	0.523(3)
0.050	0.035	0.2920(7)	0.659(4)	0.713(9)	1.48(6)	0.023(6)	0.533(3)
0.050	0.050	0.3161(7)	0.727(4)	0.89(1)	1.86(7)	0.024(6)	0.546(2)
0.070	0.015	0.2925(8)	0.657(5)	0.70(1)	1.49(7)	0.027(7)	0.528(4)
0.070	0.025	0.3086(7)	0.701(4)	0.82(1)	1.71(7)	0.026(6)	0.540(3)
0.070	0.035	0.3240(7)	0.744(4)	0.94(1)	1.97(8)	0.025(6)	0.550(2)
0.070	0.050	0.3459(7)	0.809(4)	1.13(1)	2.38(9)	0.026(6)	0.561(2)
0.070	0.070	0.3735(7)	0.894(4)	1.41(1)	3.0(1)	0.026(6)	0.574(2)
0.100	0.015	0.3397(9)	0.780(6)	1.03(2)	2.2(1)	0.032(9)	0.550(4)
0.100	0.025	0.3538(8)	0.821(5)	1.16(2)	2.5(1)	0.029(7)	0.561(3)
0.100	0.035	0.3674(7)	0.862(5)	1.30(1)	2.8(1)	0.028(6)	0.569(2)
0.100	0.050	0.3871(7)	0.924(5)	1.52(2)	3.2(1)	0.027(6)	0.579(2)
0.100	0.070	0.4123(7)	1.005(5)	1.83(2)	3.9(2)	0.026(6)	0.590(2)
0.100	0.100	0.4482(7)	1.123(6)	2.34(2)	4.9(2)	0.026(7)	0.604(1)

$(t_2, t_1) = (24, 0)$, $(32, 8)$, $(8, 16)$, and $(16, 24)$. Within each set, all the three-point functions are equivalent after proper translation in the time direction, so they are averaged after the translation. For the set A (with $|t_2 - t_1| = 16$), two equivalent regions, $0 < t < 16$ and $16 < t < 32$ are further

averaged. The averaged three-point functions are finally shifted such that the wall source for the set A and B is $(t_2, t_1) = (16, 0)$ and $(32, 8)$, respectively.

At large time separation, $|t_2 - t| \gg 1$ and $|t - t_1| \gg 1$, (8) is expected to behave as

TABLE VII. Numerical results at $m_{\text{sea}} = 0.050$ in the $Q = -2$ sector.

m_{v1}	m_{v2}	m_P	$Z_{A_4}^{\text{wall}} f_P/2$	c_0	c_1	Δ_P	$B_P^{\overline{\text{MS}}}(2\text{ GeV})$
0.015	0.015	0.177(1)	0.351(5)	0.169(6)	0.33(3)	0.00(1)	0.446(9)
0.025	0.015	0.201(1)	0.410(5)	0.240(8)	0.46(4)	0.00(1)	0.464(7)
0.025	0.025	0.223(1)	0.464(5)	0.317(9)	0.61(4)	0.00(1)	0.479(7)
0.035	0.015	0.224(1)	0.467(6)	0.32(1)	0.62(4)	0.01(1)	0.480(7)
0.035	0.025	0.244(1)	0.516(5)	0.40(1)	0.78(5)	0.01(1)	0.492(7)
0.035	0.035	0.262(1)	0.567(5)	0.50(1)	0.96(6)	0.007(9)	0.504(6)
0.050	0.015	0.254(1)	0.545(6)	0.46(1)	0.88(6)	0.01(1)	0.500(7)
0.050	0.025	0.271(1)	0.590(6)	0.55(1)	1.05(6)	0.01(1)	0.509(6)
0.050	0.035	0.288(1)	0.638(6)	0.65(1)	1.25(7)	0.008(9)	0.520(6)
0.050	0.050	0.312(1)	0.710(6)	0.83(2)	1.57(9)	0.007(9)	0.535(6)
0.070	0.015	0.289(1)	0.641(7)	0.66(2)	1.28(9)	0.01(1)	0.523(7)
0.070	0.025	0.305(1)	0.681(6)	0.76(2)	1.45(9)	0.01(1)	0.529(6)
0.070	0.035	0.320(1)	0.727(6)	0.88(2)	1.7(1)	0.01(1)	0.539(6)
0.070	0.050	0.342(1)	0.796(6)	1.08(2)	2.0(1)	0.01(1)	0.552(6)
0.070	0.070	0.370(1)	0.886(7)	1.37(3)	2.5(2)	0.00(1)	0.568(6)
0.100	0.015	0.336(1)	0.769(8)	1.00(3)	2.0(2)	0.02(2)	0.550(8)
0.100	0.025	0.350(1)	0.805(7)	1.10(2)	2.1(1)	0.01(1)	0.554(7)
0.100	0.035	0.363(1)	0.849(7)	1.25(3)	2.3(2)	0.01(1)	0.562(7)
0.100	0.050	0.383(1)	0.916(7)	1.48(3)	2.7(2)	0.00(1)	0.574(6)
0.100	0.070	0.409(1)	1.003(7)	1.82(3)	3.3(2)	0.00(1)	0.588(6)
0.100	0.100	0.444(1)	1.127(8)	2.36(4)	4.2(3)	0.00(1)	0.605(5)

TABLE VIII.   Numerical results at $m_{\text{sea}} = 0.050$ in the $Q = -4$ sector.

m_{v1}	m_{v2}	m_P	$Z_{A_4}^{\text{wall}} f_P/2$	c_0	c_1	Δ_P	$B_P^{\overline{\text{MS}}}(2 \text{ GeV})$
0.015	0.015	0.185(1)	0.378(4)	0.198(6)	0.44(3)	0.02(1)	0.451(8)
0.025	0.015	0.208(1)	0.436(5)	0.278(7)	0.62(4)	0.022(9)	0.476(6)
0.025	0.025	0.229(1)	0.482(5)	0.349(8)	0.77(4)	0.024(8)	0.489(5)
0.035	0.015	0.230(1)	0.494(5)	0.373(9)	0.82(5)	0.024(9)	0.497(5)
0.035	0.025	0.2480(9)	0.531(5)	0.437(9)	0.96(5)	0.026(8)	0.504(4)
0.035	0.035	0.2658(9)	0.578(5)	0.53(1)	1.17(6)	0.028(8)	0.515(4)
0.050	0.015	0.259(1)	0.576(5)	0.53(1)	1.17(7)	0.027(8)	0.522(5)
0.050	0.025	0.275(1)	0.604(5)	0.59(1)	1.30(7)	0.029(8)	0.523(4)
0.050	0.035	0.291(1)	0.645(5)	0.68(1)	1.51(8)	0.029(8)	0.532(4)
0.050	0.050	0.314(1)	0.711(5)	0.85(1)	1.9(1)	0.030(9)	0.546(4)
0.070	0.015	0.294(1)	0.676(6)	0.77(2)	1.7(1)	0.032(9)	0.547(5)
0.070	0.025	0.308(1)	0.695(6)	0.81(2)	1.8(1)	0.032(9)	0.545(4)
0.070	0.035	0.322(1)	0.732(6)	0.91(2)	2.0(1)	0.031(9)	0.551(4)
0.070	0.050	0.343(1)	0.794(6)	1.09(2)	2.4(1)	0.03(1)	0.563(5)
0.070	0.070	0.371(1)	0.878(6)	1.37(2)	3.0(2)	0.03(1)	0.577(5)
0.100	0.015	0.340(1)	0.810(7)	1.16(2)	2.7(2)	0.04(1)	0.575(5)
0.100	0.025	0.352(1)	0.820(6)	1.18(2)	2.7(2)	0.04(1)	0.569(5)
0.100	0.035	0.365(1)	0.852(6)	1.28(2)	2.9(2)	0.03(1)	0.574(5)
0.100	0.050	0.384(1)	0.910(7)	1.48(2)	3.2(2)	0.03(1)	0.583(5)
0.100	0.070	0.409(1)	0.990(7)	1.79(3)	3.8(3)	0.02(1)	0.595(5)
0.100	0.100	0.444(1)	1.110(8)	2.31(4)	4.7(4)	0.02(1)	0.610(5)

$$\text{eq.}(8) \rightarrow V_3 c_0 e^{-m_P(t_2-t_1)} + V_3 c_1 e^{-m_P N_t - \Delta_P(t_2-t_1)/2} \cosh\left[\left(2m_P + \Delta_P\right)\left(t - \frac{t_2 + t_1}{2}\right)\right] + V_3 c_2 e^{-(m_{P'} + m_P)(t_2-t_1)/2} \cosh$$

$$\times \left[\left(m_{P'} - m_P\right)\left(t - \frac{t_2 + t_1}{2}\right)\right] + V_3 c_3 e^{-m_P N_t - (m_{P'} - m_P + \Delta'_P)(t_2-t_1)/2} \cosh\left[\left(m_{P'} + m_P + \Delta'_P\right)\left(t - \frac{t_2 + t_1}{2}\right)\right]. \quad (10)$$

The meaning of each term is explained in the following. The first term in (10) contains the hadron matrix element relevant to the calculation of B_K, and $c_0 = (Z_{A_4}^{\text{wall}})^2 \times \langle \bar{P} | O_{L_\mu L_\mu}^{\text{lat}} | P \rangle / (2m_P)^2$. The schematic diagram corresponding to this contribution is shown in Fig. 3. While this contribution does not depend on t, in the real data, as shown in Fig. 4, the three-point function depends on t, and the dependence is more pronounced for the lighter meson (left). To describe this t-dependence, we incorporate three additional terms: a contribution of a kaon wrap-

ping around the lattice in the time direction, an excited state contamination, and a mixture of a wrapping kaon and an excited state. The diagrams corresponding to these three contributions are depicted in Fig. 5. The second term in (10) represents a wrapping kaon contribution [Fig. 5 (top)], and c_1 contains the transition amplitude of a two-kaon state $|P, P\rangle$ to the vacuum, $\langle 0 | O_{L_\mu L_\mu}^{\text{lat}} | P, P \rangle$. $\Delta_P = E_{\text{total}} - 2m_P$ denotes the total energy difference between an interacting and noninteracting two-kaon system, and is extracted through the fit. The third term describes the transition
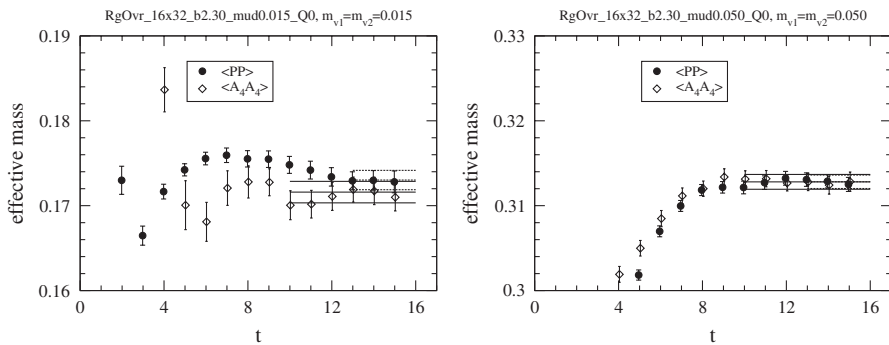

FIG. 1.   Effective mass plots for the pseudoscalar meson with $m_{\text{sea}} = m_{v1} = m_{v2}$. The plots for $m_{\text{sea}} = 0.015$ (left) and 0.050 (right) are shown as representatives.
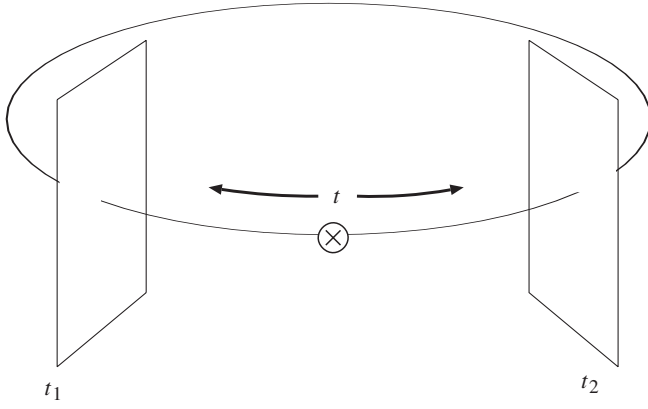
FIG. 2.   The setup of two wall sources at t_1 and t_2 and the local operator at t to calculate the three-point function.
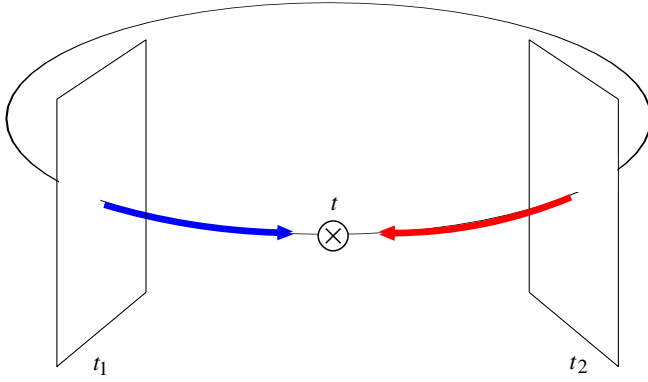

FIG. 3 (color online).   The contribution of the three-point function relevant to the calculation of B_K.

amplitude between the ground state $|P\rangle$ and the first excited state $|\bar{P}'\rangle$, hence c_2 contains $\langle \bar{P}' | O^{\text{lat}}_{L_\mu L_\mu} | P \rangle$ [Fig. 5 (middle)]. The excited state mass $m_{P'}$ is extracted from the two-point function with a point source and a point sink through a double cosh fit using the fixed ground state mass. Finally the fourth term represents the mixture contribution [Fig. 5 (bottom)].

The set A and B are fitted simultaneously to obtain c_0 with m_P fixed to the value extracted from the two-point function. In the fit, two cases are examined, one taking the excited state contaminations, i.e., the c_2 and c_3 terms in (10), into account and the other not. The c_1 term is always included. In both cases, the fit range dependence is investigated. For later use, the fit ranges $[t_{\min}, t_{\max}]$ for the set A and B are parametrized as

$$[t_{\min}, t_{\max}] = \begin{cases} [8 - dt, 8 + dt] & \text{for set A,} \\ [16 - dt, 24 + dt] & \text{for set B.} \end{cases} \quad (11)$$

Then $8 - dt$ corresponds to the time separation between an end of the fit range and the nearest source operator.

We first perform an uncorrelated simultaneous fit without the c_2 and c_3 terms. The solid curves in Fig. 4 represent the results for $dt = 2$. The numerical results of c_0, c_1, and Δ_P for $dt = 2$ are tabulated in Tables I, II, III, IV, V, VI, VII, and VIII. As seen from Fig. 4, the fit results are on the top of the data within the error, and the χ^2/dof values in the fit are acceptable and in the range of [0.01, 0.2]. Although as seen from the table Δ_P is not determined very well especially when the quark is light, the obtained values for Δ_P are reasonably consistent with those in [30], in which Δ_P is calculated on the same configurations at $m_{\text{sea}} = m_{v1} = m_{v2}$ on the way to obtaining the $I = 2$ π-π scattering length, and is determined to a better precision. The lattice B-parameter for a general pseudoscalar meson, which we call B^{lat}_P in the following, is then obtained through

$$B^{\text{lat}}_P = \frac{3}{8}\left(\frac{2}{Z^{\text{wall}}_{A_4} f_P}\right)^2 \times \frac{(Z^{\text{wall}}_{A_4})^2 \langle \bar{P} | O^{\text{lat}}_{L_\mu L_\mu} | P \rangle}{(2m_P)^2}, \quad (12)$$

where the first and second factors are obtained from the two- and three-point functions, respectively. By varying dt, we obtain the dt-dependence of B^{lat}_P in Fig. 6 (open symbols), where the data with $m_{\text{sea}} = m_{v1} = m_{v2} = m_q$ are shown. The results at $dt = 2$ are indicated by the solid horizontal lines in the figure. It is seen that B^{lat}_P systematically increases at large dt with dt while it remains unchanged for $dt \lesssim 2$.
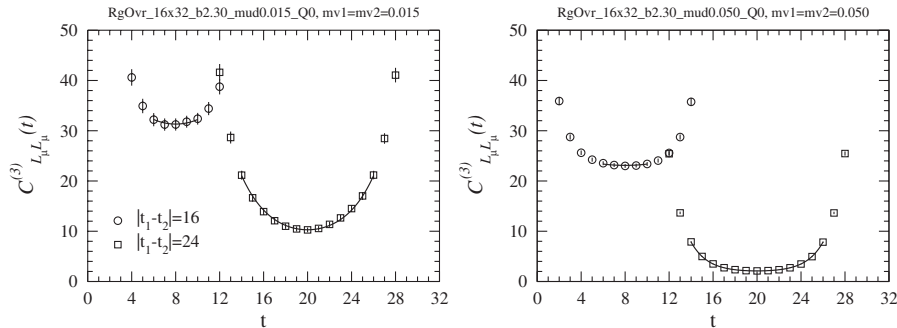

FIG. 4. t-dependence of the three-point functions. The left is for $m_{\text{sea}} = m_{v1} = m_{v2} = 0.015$, and the right for 0.050. The fit ranges are $[t_{\min}, t_{\max}] = [6, 10]$ and $[14, 26]$ for the set A and B, respectively.
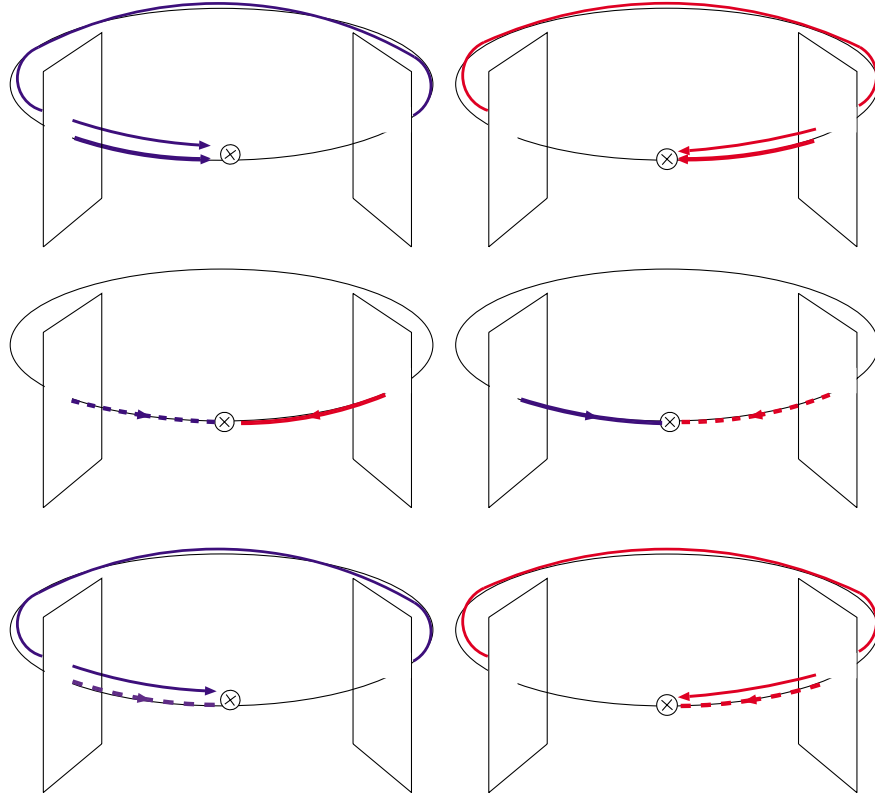
FIG. 5 (color online). Possible contaminations containing a wrapping or an excited state. The solid lines represent the kaon, and the dashed lines the first excited state.

To make an analysis including the c_2 and c_3 terms, we use the first excited state mass $m_{P'}$ extracted from the two-point function with the point source and point sink. Through a double cosh fit with a fixed ground state mass, we obtain Fig. 7, which shows the first excited state mass $m_{P'}$ as a function of $m_{\text{sea}} = m_{v1} = m_{v2} = m_q$. Although the statistical error is sizable, $m_{P'}$ reasonably extrapolates to the experimentally measured value of the excited state mass of $\pi(1300)$. In the following fits, $m_{P'}$ is fixed to the value thus extracted. As seen from (10), Δ'_P always appears in the combination $m_{P'} + \Delta'_P$. According to some trial fits in which Δ'_P is treated as a free parameter, it turned out that Δ'_P is not determined well and its size is similar to or even smaller than the statistical error of $m_{P'}$. Therefore, in the following analysis, whose purpose is to test the stability against the fit range, we set Δ'_P to zero. The simultaneous fit to (10) including the c_2 and c_3 terms is carried out with varying dt as before, and the resulting dt-dependence of B_P^{lat} is shown in Fig. 6 (filled symbols). It turns out that in this case B_P^{lat} does not depend on dt and its value is consistent with the open symbol at $dt \leq 2$ for all the quark masses.

To show the significance of each term in (10), each contribution is separately plotted with a logarithmic scale in Fig. 8. We find that the contributions from the c_2 and c_3 terms in (10) are always smaller than the others. An exception is the set A at $m_{\text{sea}} = 0.050$ (right), in which the c_2 term is as large as the c_1 term. But in this case the size of these contributions is only a few % of the relevant term to extract B_P^{lat}. Another possible contamination, which has not been discussed so far, is the one containing the transition amplitude between the first excited states, $\langle \bar{P}' | O_{L_\mu L_\mu}^{\text{lat}} | P' \rangle$. Using $m_{P'}$ obtained above, its effect to B_P^{lat} is estimated to be less than 0.03%, and so is neglected.

From the above observations, in the following analysis we use B_P^{lat} obtained at $dt = 2$ without the c_2 and c_3 terms.

C. Nonperturbative matching

We adopt the RI/MOM scheme [31] to calculate the matching factor. We follow the standard method, which is briefly described in the following. In this subsection, we consider the renormalization of the operator of the chiral structure $VV + AA$, $(\bar{q}_1 \gamma_\mu q'_2 \bar{q}_1 \gamma_\mu q'_2) + (\bar{q}_1 \gamma_\mu \gamma_5 q'_2 \bar{q}_1 \gamma_\mu \gamma_5 q'_2)$, rather than $O_{L_\mu L_\mu}$ defined in (9), since in the presence of chiral symmetry the matching factors for these two operators are equivalent. Fixing the gauge to the Landau gauge, we first calculate the five-point vertex function (or equivalently the amputated five-point function) for the $VV + AA$ operator, where four external off-shell momenta are set to a common value. By applying a proper spin-color projection, the vertex function is de-
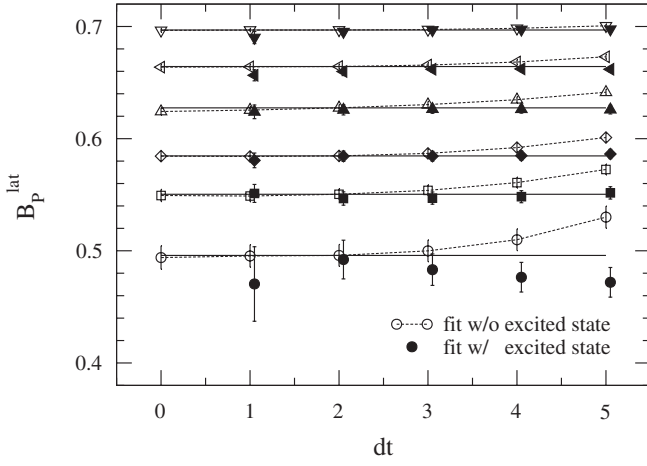
FIG. 6. Fit range dependence of B_P^{lat}. The open (filled) symbols are obtained by fitting the data to (10) without (with) the c_2 and c_3 terms. The horizontal solid lines represent the value of the open symbol at $dt = 2$. This analysis is performed only at the unquenched points $(m_{v1} = m_{v2} = m_{\text{sea}})$. The quark mass increases from bottom to top.
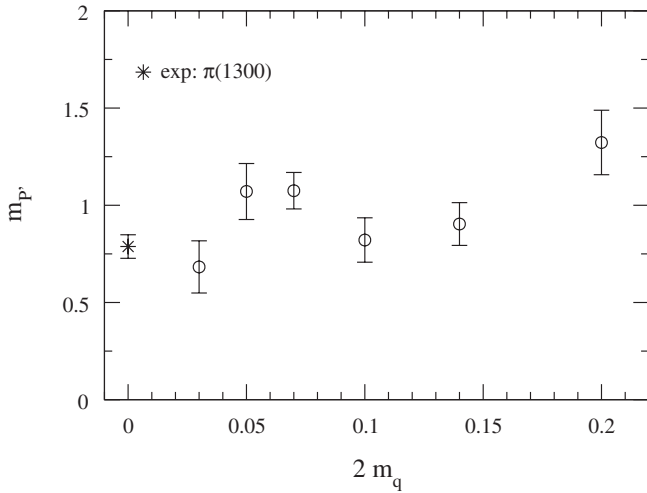

FIG. 7. The quark mass dependence of the first excited state mass, $m_{P'}$ (circles) in the lattice unit. The experimental value of $\pi(1300)$ is also shown.

composed into five different structures, $(VV \pm AA)$, $(SS \pm PP)$, TT, where V, A, S, P, T denote vector, axial-vector, scalar, pseudoscalar, and tensor bilinears, respectively. In Fig. 9, the lattice momentum dependence of the multiplicative part (circles) and the mixing part (other symbols) are shown. As is guaranteed by the exact chiral symmetry, the nonmultiplicative contributions are strongly suppressed and vanish asymptotically as momentum becomes large. By imposing the renormalization condition that the $VV + AA$ component of the renormalized vertex function be equal to the tree-level value, we obtain $Z_q^{-2} Z_{VV+AA}$ with Z_q the quark wave function renormalization. We also calculate the vertex function for the axial-vector current with the same momentum configurations to obtain $Z_q^{-1} Z_A$. Taking a ratio of the multiplicative part of the five-point vertex function to a square of the vertex function for the axial-vector current, we obtain $Z_{B_K}^{\text{RI/MOM}} = Z_{VV+AA}/Z_A^2$ at each quark mass and each momentum.

The momentum ap_μ is defined by $ap_\mu = 2\pi n_\mu/L_\mu$, where L_μ is the number of total lattice sites in the μ direction and n_μ is an integer. While n_μ can take the value in the range of $[-(L_\mu/2) + 1, (L_\mu/2)]$, in order to avoid the large discretization error we restrict the range to that satisfying $ap_\mu < 1$. Namely, n_μ can only take $n_i = \{-2, -1, 0, 1, 2\}$ for $i = x$, y, z and $n_t = \{-5, -4, -3, -2, -1, 0, 1, 2, 3, 4, 5\}$. Then the maximum value for $(ap)^2$ used in the following analysis is about 2.81.

The chiral extrapolation of $Z_{B_K}^{\text{RI/MOM}}$ is made linearly in the quark mass as shown in Fig. 10. A clear dependence on quark mass is observed at relatively small $(ap)^2$ while the dependence vanishes at larger $(ap)^2$. After the chiral limit at each lattice momentum, we finally obtain $Z_{B_K}^{\text{RI/MOM}}$ shown in Fig. 11 (open circles). In [11], possible nonperturbative contaminations are discussed in detail. With the momentum setup commonly used in the RI/MOM scheme, some nonperturbative effects may be enhanced in the small momentum region. They are responsible for the linear dependence on the quark mass in this region. To avoid such contaminations, in the following analysis we restrict the data point to those of $(ap)^2 > 1.2337$, where the

FIG. 8. The size of each contribution. The plots for $m_{\text{sea}} = 0.015$ (left) and 0.050 (right) are shown as representatives. See the text for details.
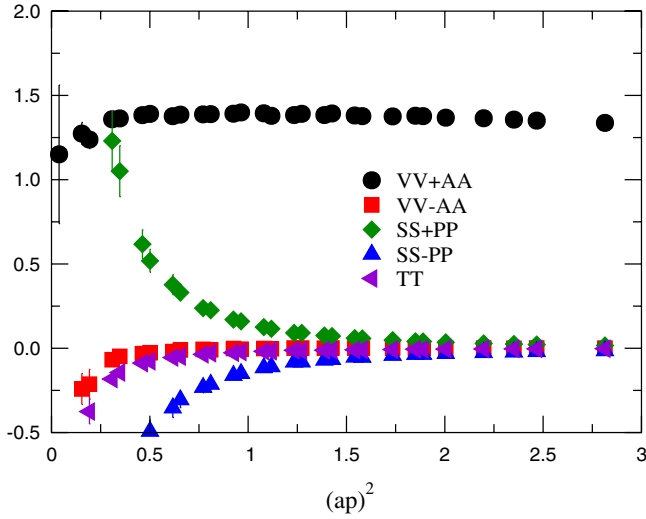
FIG. 9 (color online). Lattice momentum dependence of each component of the five-point vertex function for $m_q = 0.015$.
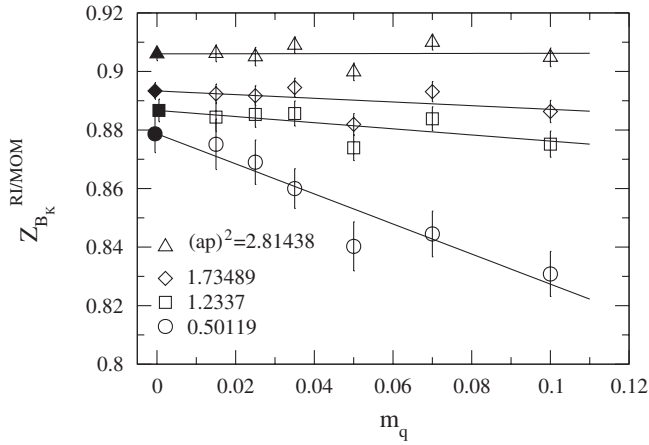

FIG. 10. Chiral extrapolation of $Z_{B_K}^{RI/MOM}$ at several representative momenta.
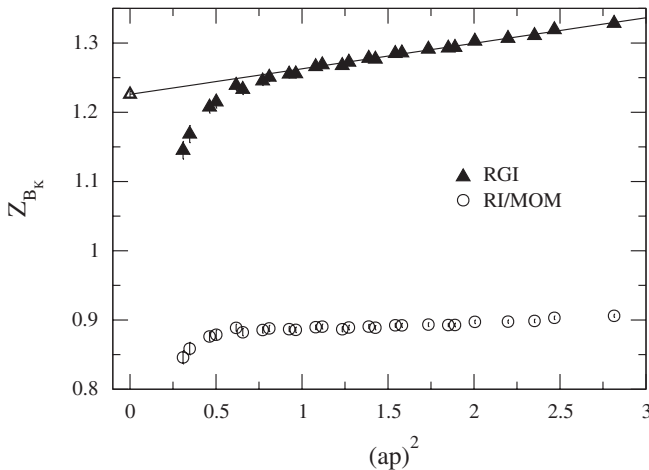

FIG. 11. $Z_{B_K}^{RI/MOM}$ in the chiral limit and $Z_{B_K}^{RGI}$ as a function of the external state momentum squared.

linear slope is consistent with zero within 2 standard deviations.

From $Z_{B_K}^{RI/MOM}(p^2)$ the renormalization group invariant (RGI) factor $Z_{B_K}^{RGI}$ is obtained by

$$Z_{B_K}^{RGI} = w_{RI/MOM}^{-1}(\mu^2) Z_{B_K}^{RI/MOM}(\mu^2), \qquad (13)$$

where

$$w_{RI/MOM}(\mu^2) = (\alpha_s(\mu^2))^{\gamma_0/2\beta_0} \left[1 - \frac{\alpha_s(\mu^2)}{4\pi} J_{RI/MOM} \right], \qquad (14)$$

is the running factor due to the anomalous dimension at the next-to-next-to-leading order. $\gamma_0 = 4$ and

$$J_{RI/MOM} = \frac{-(23931 - 2862N_f + 128N_f^2)}{6(33 - 2N_f)^2} + 1 + 8\ln2, \qquad (15)$$

which is calculated in [32]. We use the running coupling constant at the same order given by

$$\alpha_s(\mu^2) = \frac{4\pi}{\beta_0 L} \left[1 - \frac{\beta_1}{\beta_0^2} \frac{\ln L}{L} \right], \qquad (16)$$

with $\beta_0 = \frac{33-2N_f}{3}$, $\beta_1 = 102 - 10N_f - \frac{8}{3}N_f$, and $L = \ln(\mu^2/\Lambda_{QCD}^2)$. In [33], Λ_{QCD} for $N_f = 2$ in the $\overline{MS}$ scheme is calculated to be 245(16)(16) MeV assuming $r_0 = 0.5$ fm. By summing up the two errors and converting to $r_0 = 0.49$ fm, we obtain $\Lambda_{QCD} = 250(33)$ MeV which we will use in the following analysis.

The resulting $Z_{B_K}^{RGI}$ is shown in Fig. 11 (filled triangles). $Z_{B_K}^{RGI}$ must be independent of the renormalization scale up to neglected higher order effects. The remaining scale dependence due to the neglected higher order effects is estimated as follows. In our momentum region, the factor $1/w_{RI/MOM}(\mu^2)$ is well approximated by a linear function of $(ap)^2$ as $w_0[1 + w_1(ap)^2]$. The slope w_1 determined with two points $(ap)^2 = 1.2337$ and $2.814\,38$ is 0.017 or 0.022, with and without the $O(\alpha_s)$ term in (14), respectively. From the difference of w_1 between these two cases, we deduce that the $O(\alpha_s^2)$ correction affects w_1 by less than 0.005. On the other hand, fitting the data to a linear function of $(ap)^2$, we obtain $Z_{B_K}^{RGI} = 1.226(5) \times [1 + 0.030(2) \times (ap)^2]$. Therefore, we conclude that the remaining $(ap)^2$ dependence is dominated by the $O(a^2p^2)$ discretization effects, which are removed by a linear extrapolation to $(ap)^2 = 0$ as shown in Fig. 11. We observe a clear nonzero slope in $(ap)^2$ for $Z_{B_K}^{RGI}$, but the coefficient is sufficiently small to rely on the extrapolation.

To follow the standard convention, the matching factor is converted to that in the $\overline{MS}$ scheme using

$$Z_{B_K}^{\overline{MS}}(\mu^2) = w_{\overline{MS}}(\mu^2) Z_{B_K}^{RGI}, \qquad (17)$$

where $w_{\overline{\text{MS}}}(\mu^2)$ is obtained from (14) by replacing $J_{\text{RI/MOM}}$ with [32]

$$J_{\overline{\text{MS}}} = \frac{-(23931 - 2862N_f + 128N_f^2)}{6(33 - 2N_f)^2} + \frac{17}{3}. \quad (18)$$

We obtain $w_{\overline{\text{MS}}}(\mu^2) = 0.7086$ at $\mu = 2$ GeV.

In the whole procedure, the largest uncertainty comes from the perturbative running. The matching factor at a given scale μ in the RI/MOM scheme is obtained nonperturbatively, but its conversion to other schemes is not. The systematic uncertainty is then estimated by the size of the correction of the highest order included (next-to-leading order in this work), which is 0.071 for $Z_{B_K}^{\text{RGI}}$ and 0.020 for $Z_{B_K}^{\overline{\text{MS}}}(2 \text{ GeV})$. The uncertainty of Λ_{QCD} gives ± 0.013 for $Z_{B_K}^{\text{RGI}}$ and ± 0.0002 for $Z_{B_K}^{\overline{\text{MS}}}(2 \text{ GeV})$. These systematic errors are added in quadrature. Finally we obtain

$$Z_{B_K}^{\text{RGI}} = 1.224(5)(72), \qquad Z_{B_K}^{\overline{\text{MS}}}(2 \text{ GeV}) = 0.867(3)(20),$$
$$(19)$$

where the first error is statistical and the second one is systematic. The results for the B-parameter in the $\overline{\text{MS}}$ scheme at $\mu = 2$ GeV, $B_P^{\overline{\text{MS}}}(2 \text{ GeV})$, are given in Tables I, II, III, IV, V, VI, VII, and VIII.

IV. TEST WITH NLO PQCHPT

Before extrapolating the lattice data to the physical kaon mass ($m_{\nu 1} = m_{\text{sea}} \to m_{ud}^{\text{phys}}$, $m_{\nu 2} \to m_s^{\text{phys}}$), we test whether the quark mass dependence of B_P is consistent with the NLO PQ ChPT prediction. In other words we try to identify the quark mass region, where the lattice results are well described by ChPT. We restrict the data points used to those which satisfy $m_{\text{sea}} \leq m_{\text{valence}}$ for the reason described below.

In [34], the finite volume effect (FVE) to B_K is studied to NLO in the framework of finite volume PQChPT, where the "kaon" consists of a light quark with mass $m_{\nu 1}$ and the physical strange quark mass with $m_{\nu 2}$ fixed to m_s^{phys}. Its

numerical results indicate that the FVE is more profound as $m_{\nu 1}$ vanishes while m_{sea} is fixed. This can be deduced from the NLO PQChPT formula for B_K in the infinite volume alone, because it contains the term proportional to $m_{\text{sea}} \ln(m_{\nu 1}/m_{\nu 2})$ and the loop integral leading to this term is expected to be sensitive to the infrared cutoff, or equivalently to the size of the spatial volume. Then the chiral expansion with $m_{\nu 1} \ll m_{\text{sea}}$ becomes unlikely to converge quickly and hence less reliable. Quantitatively, the estimate of the FVE to B_K in [34] gives about 3% for $m_{\nu 1} \sim m_s^{\text{phys}}/5$ and $m_{\nu 2} = m_{\text{sea}} \sim m_s^{\text{phys}}$ and so appears to be under control. However it is pointed out in [35] (and cautioned in [34]) that at the NLO the FVE could be significantly underestimated for m_π and f_π. For example, the NLO estimate of the FVE to f_π gives about 2% correction at our lightest unquenched point while the inclusion of NNLO gives 4%–5%. It should be noted that this study is made at the unquenched points ($m_{\text{sea}} = m_{\nu 1} = m_{\nu 2}$). Therefore it could be worse when $m_{\nu 1} \ll m_{\text{sea}} \sim m_{\nu 2}$ because of the above reason. Motivated by these observations, in the following analysis we include the data points only when $m_{\text{sea}} \leq m_{\text{valence}}$.

In this test, we focus on the data points consisting of degenerate quarks ($m_{\nu 1} = m_{\nu 2}$) for simplicity. The NLO PQChPT prediction for B_P with degenerate valence quarks is [34,36],

$$B_P = B_P^\chi \left[1 - \frac{6m_P^2}{(4\pi f)^2} \ln\left(\frac{m_P^2}{\mu^2}\right) \right] + (b_1 - b_3)m_P^2 + b_2 m_{ss}^2, \quad (20)$$

where m_{ss} is the pseudoscalar meson mass with $m_{\nu 1} = m_{\nu 2} = m_{\text{sea}}$ and B_P^χ, f, $(b_1 - b_3)$, and b_2 are free parameters. f is the tree-level pion decay constant in the $f_\pi \sim 130$ MeV normalization, and is the only parameter which controls nonlinear dependence of B_P on the pseudoscalar meson mass squared. In the fit, μ is set to 1 GeV. The numerical data are fitted to (20) with a varying fit range.

The fit results are summarized in Table IX (top) and shown in Fig. 12 (left). While all fit ranges tested give acceptable χ^2/dof, f monotonically increases as the fit

TABLE IX. Results of the NLO PQChPT fit. In both fits, μ is set to 1 GeV.

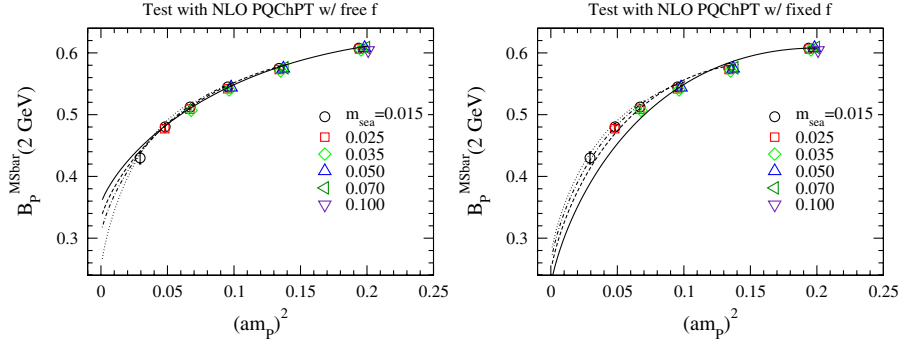| Fit range in m_{sea}	χ^2/dof	B_P^χ	$b_1 - b_3$	b_2	f
Fit results with unfixed f					
[0.015, 0.035]	0.21	0.26(6)	0.3(6)	−0.2(3)	0.06(2)
[0.015, 0.050]	0.25	0.31(3)	0.9(1)	−0.1(1)	0.09(2)
[0.015, 0.070]	0.33	0.33(2)	1.03(3)	−0.09(8)	0.101(8)
[0.015, 0.100]	0.75	0.36(1)	1.04(3)	−0.05(4)	0.120(6)
Fit results with f fixed to 0.0659					
[0.015, 0.035]	0.15	0.27(1)	0.5(2)	−0.2(3)	—
[0.015, 0.050]	0.46	0.260(5)	0.76(6)	−0.1(1)	—
[0.015, 0.070]	2.5	0.246(3)	1.07(3)	−0.09(8)	—
[0.015, 0.100]	13.5	0.224(2)	1.42(2)	−0.03(5)	—

FIG. 12 (color online). $B_P^{\overline{\mathrm{MS}}}(2 \text{ GeV})$ as a function of valence pion mass squared. The data are fit to the NLO PQChPT formula with an unfixed f (left) and the fixed $f = 0.0659$ (right). The different symbols denote different sea quark masses. Several curves are obtained with different fit ranges and show the ones extrapolated to $m_{\mathrm{sea}} = 0$.

range is extended. f's obtained from the two narrowest ranges are consistent with each other within 1 standard deviation, and also consistent with a naive expectation $100 \sim 130$ MeV. We also attempt another fit fixing f to 0.0659, which corresponds to 110 MeV obtained in our separate calculation [15]. The numerical results and plot are given in Table IX (bottom) and in Fig. 12 (right), respectively. The χ^2/dof is acceptable for the two narrowest fit ranges, and the results for other fit parameters are consistent with the values obtained without fixing f. From these observations, we conclude that the data for $m_q \leq 0.050$ are inside

the NLO regime while the data at around the strange quark mass are not.

V. EXTRACTION OF B_K

Since the NLO PQChPT formula describes the data only up to about a half of the physical strange quark mass, to extract B_K at physical quark masses from the data, it is necessary to modify the NLO PQChPT formula. We incorporate an analytic term into the original NLO PQChPT formula [10,34,36] as

$$B_{12} = B_{12}^\chi \left[1 - \frac{2}{(4\pi f)^2} \left\{ m_{ss}^2 + m_{11}^2 - \frac{3m_{12}^4 + m_{11}^4}{2m_{12}^2} + m_{12}^2 \left(\ln\left(\frac{m_{12}^2}{\mu^2}\right) + 2\ln\left(\frac{m_{22}^2}{\mu^2}\right) \right) - \frac{1}{2}\left(\frac{m_{ss}^2(m_{12}^2 + m_{11}^2)}{2m_{12}^2} \right. \right. \right.$$
$$\left. \left. \left. + \frac{m_{11}^2(m_{ss}^2 - m_{11}^2)}{m_{12}^2 - m_{11}^2} \right) \ln\left(\frac{m_{22}^2}{m_{11}^2}\right) \right\} \right] + b_1 m_{12}^2 + b_3 m_{11}^2 \left(-2 + \frac{m_{11}^2}{m_{12}^2} \right) + b_2 m_{ss}^2 + d_1 (m_{12}^2)^2, \tag{21}$$

where m_{ij} is the pseudoscalar meson mass consisting of valence quarks i and j. In the limit of $m_{v1} = m_{v2}$, the above formula without the last term reduces to (20). The formula (21) without the last term is the NLO PQChPT prediction for nondegenerate valence quarks [10,34,36], and the last term is added to interpolate the data in the heavy valence quark mass region. Since the modification is used to interpolate the existing data in the heavier valence quark mass region, its precise form is irrelevant to the final result. Actually we have confirmed that introducing the

other term $d_2(m_{11}^2 m_{22}^2)$ into the formula changes the final result by 0.2% at most.

The fit is performed with four data sets, each of which includes the data of three, four, five, or six lightest sea quarks. All the data satisfying $m_{\mathrm{sea}} \leq \min(m_{v1}, m_{v2})$ are included in the fit. Numerical results and the plots are given in Table X and Fig. 13, respectively. Solid curves in Fig. 13 represent the fit result extrapolated to the point where one of the valence quark mass and the sea quark mass (m_{sea}) are equal to the physical u, d mass (m_{ud}^{phys}) while the

TABLE X.   Results of fitting to the NLO PQChPT plus a quadratic term. In the fits, μ is set to 1 GeV.

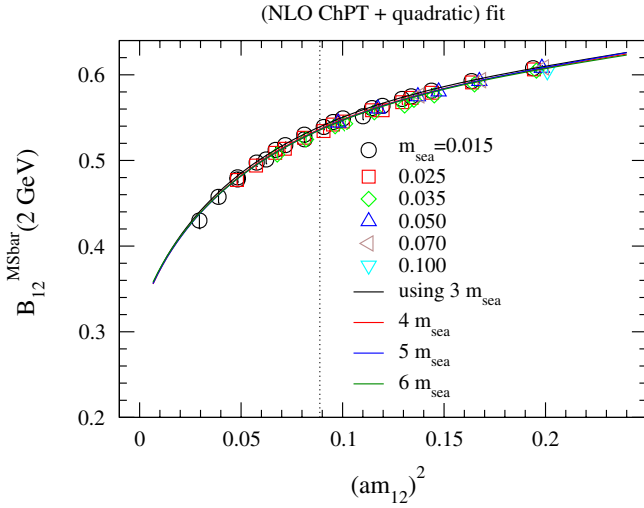| Fit range in m_{sea}	χ^2/dof	B_P^χ	b_1	b_2	b_3	d_1	f	$B_K^{\overline{\mathrm{MS}}}(2 \text{ GeV})$
Fit results with unfixed f								
[0.015, 0.035]	0.1	0.31(2)	−0.5(3)	−0.15(10)	−0.11(3)	4.0(9)	0.079(8)	0.539(7)
[0.015, 0.050]	0.4	0.31(2)	−0.4(3)	−0.06(5)	−0.10(3)	3.9(1.0)	0.080(9)	0.537(4)
[0.015, 0.070]	0.5	0.31(2)	−0.4(3)	−0.02(3)	−0.09(4)	3.9(1.0)	0.081(9)	0.536(4)
[0.015, 0.100]	0.5	0.31(2)	−0.3(3)	−0.03(2)	−0.09(4)	3.5(1.2)	0.083(10)	0.535(4)

FIG. 13 (color online). m_{12}^2 dependence of $B_{12}^{\overline{\text{MS}}}$(2 GeV). The different symbols correspond to different m_{sea}. The solid curves represent B_P with m_{sea} and $m_{\nu1}$ extrapolated to m_{ud}^{phys}. The vertical line indicates the location of physical m_K.

other valence quark mass is free. Therefore the lines show the strange (or heavier valence) quark mass dependence of the B-parameter. Since the four curves obtained with different data sets are indistinguishable from each other and all the data used in the fit are on top of each other, we may conclude that the difference between degenerate and nondegenerate data is negligible for B_P. As seen from Table X, B_P^{χ}'s, b_2's, and f's for all the fit ranges are reasonably consistent with those obtained for the two narrowest fit ranges with unfixed f in the NLO test shown in Table IX (top). Interpolating to physical m_K^2, we obtain $B_K^{\overline{\text{MS}}}$(2 GeV), listed in Table X. We take $B_K^{\overline{\text{MS}}}$(2 GeV) = 0.537(4), which is the result with the fit range [0.015, 0.050], as the central value. The difference from the others (± 0.002) is ignored as it is much smaller than other systematic errors.

VI. SYSTEMATIC ERRORS

A. Finite volume effects

With our lattice size and the lightest pion mass, $m_\pi L$ is slightly smaller than 3, for which one expects sizable finite volume effects. One of such effects, which is special in the partially quenched theory and becomes significant when $m_{\nu1}, m_{\nu2} < m_{\text{sea}}$, has been eliminated by omitting a potentially dangerous data set. If we apply the estimate based on the finite volume NLO PQChPT analysis [34] to our lattice setup with $L = 2$ fm, the finite size effect is estimated to be less than 1% over all the data points we have included in the fit. However, as mentioned before, the NNLO analysis revealed that the NLO analysis could significantly underestimate the effect for m_π and f_π [35]. Unfortunately, the

NNLO calculation of B_K is not available. Therefore, we add 5% uncertainty, which is the NNLO estimate on f_π at our lightest quark mass [15], as a conservative upper bound of the finite volume effect.

B. Fixing topology

In our calculation there is a finite volume effect of a different origin, i.e., the fixed topological charge. This effect is suppressed for large volumes as $1/V$, and is calculable provided that the topological susceptibility and the θ-dependence of the quantity of interest are known [14,37]. The topological susceptibility is calculated on the same set of lattices [18]. Within the framework of ChPT, it can be shown that the most significant θ-dependence of the physical quantities is that of pion mass and other quantities are affected through it. We estimate the size of the effect on B_P as

$$\sim B_P^{\chi} \frac{m_P^2}{(4\pi f)^2} \frac{1}{\langle Q^2 \rangle}\left(1 - \frac{Q^2}{\langle Q^2 \rangle}\right), \qquad (22)$$

which appears at the next-to-leading order of ChPT. Here, $\langle Q^2 \rangle = \chi_t V_4 \sim 10$ at $m_q = 0.05$ [18] and V_4 is the four-dimensional volume. At this sea quark mass, the correction to the $Q = 0$ result is estimated to be 1.4%, and the difference between $Q = 0$ and $-2(-4)$ to be 0.6% (2.4%). To see whether this expected difference is seen or not, three results of B_P at $m_q = 0.05$ in the $Q = 0$, -2, -4 sectors are compared in Fig. 14. Since the size of the statistical error for the measured B_P is about 1% or so as shown in the figure, we do not expect clear systematic Q-dependence of B_P, that is confirmed by the numerical data. From this observation, we can safely assume that (22) gives a reasonable estimate. We quote 1.4% as an estimate for the systematic error due to fixing the topological charge. A more complete analysis is available for f_π [15], for which
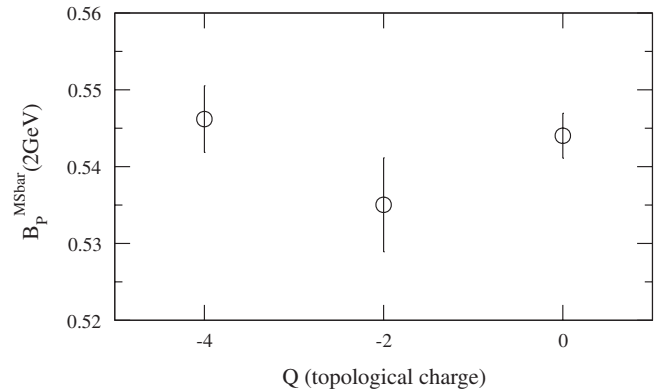

FIG. 14. Comparison of $B_P^{\overline{\text{MS}}}$(2 GeV) at $m_{\text{sea}} = 0.05$ with three different topological charges: $Q = 0$, -2, -4.

the effect of fixing the topological charge is estimated to be about 1% or less depending on the quark mass.

C. Other systematic errors

In addition to the above errors, we estimated 2% uncertainty in the determination of $Z_{B_K}^{\overline{\text{MS}}}(2\ \text{GeV})$. Since the calculation is made only at one lattice spacing, a reliable estimate of the scaling violation is difficult. There is, however, an indication that the overlap fermion formulation has relatively small scaling violation within the quenched calculation of B_K [38], where no significant dependence on the lattice spacing was observed between $1/a \sim 2.2$ GeV and 1.5 GeV. Even at a fixed lattice spacing, the use of a different input to fix the lattice spacing could lead to an appreciable change of B_K because B_K has a significant dependence on the squared meson mass $(am_{12})^2$ as seen in Fig. 13. It turns out that if one changes $1/a$ by $\pm 5\%$ for instance, B_K is changed by $\mp 5\%$.

This calculation is made with two flavors of dynamical quarks, and the strange quark is quenched. In [9,10], the RBC collaboration estimate B_K with two and three dynamical flavors using the domain-wall lattice fermion formalism. While no clear dependence on the number of dynamical flavors is seen between these two calculations, we cannot draw a definite conclusion at the moment as these two calculations used different gauge actions. Therefore, we leave the estimate of the systematic error due to the missing strange quark contribution to the sea for future works.

Summing up the estimates of the systematic errors due to finite volume effects (5%), fixing topology (1.4%), the matching factor (2%), and the scale setting (5%) in quadrature, we quote our result of the $N_f = 2$ calculation obtained at $1/a \sim 1.67$ GeV as

$$B_K^{\overline{\text{MS}}}(2\ \text{GeV}) = 0.537(4)(40),\qquad (23)$$

where the first and the second errors are statistical and systematic. Notice that the systematic error shown here does not include those due to the scaling violation and neglecting the dynamical strange quark.

VII. SUMMARY

We performed a dynamical overlap fermion calculation of B_K for the first time. Although the three-point functions are contaminated by the wrapping-around kaons and the excited states because of the short temporal extent of our lattice, thanks to the low-mode averaging the statistical signal is substantially improved so that we could extract the meson and antimeson transition amplitude accurately.

Using the extracted values of the B-parameter, consistency with the NLO PQChPT prediction for B_K is tested. It turns out that the NLO prediction well describes the measured B_P up to around a half of the strange quark mass. By extrapolating B_P to the physical m_K, we obtain (23), where the uncertainties from the ordinary finite volume effect, fixing topology, and renormalization constant are included in the systematic error.

The next step to do is the determination of B_K in three-flavor QCD. The generation of configurations with three flavors of dynamical overlap fermions is underway [24]. With this calculation, the effect of quenching the strange quark is removed. We are planning a study of the finite volume effects in the three-flavor calculation by performing the calculation with two different volumes. Then the dominant uncertainties in this calculation would be eliminated.

ACKNOWLEDGMENTS

[1] W. M. Yao *et al.* (Particle Data Group), J. Phys. G **33**, 1 (2006).

[2] For the full expression, see G. Buchalla, A. J. Buras, and M. E. Lautenbacher, Rev. Mod. Phys. **68**, 1125 (1996).

[3] J. M. Flynn, F. Mescia, and A. S. B. Tariq (UKQCD Collaboration), J. High Energy Phys. 11 (2004) 049.

[4] F. Mescia, V. Gimenez, V. Lubicz, G. Martinelli, S. Simula, and C. Tarantino, Proc. Sci., LAT2005 (2006) 365 [arXiv:hep-lat/0510096].

[5] S. Aoki *et al.* (JLQCD Collaboration), Phys. Rev. Lett. **80**, 5271 (1998).

[6] A. Ali Khan *et al.* (CP-PACS Collaboration), Phys. Rev. D **64**, 114506 (2001).

[7] T. Blum *et al.* (RBC Collaboration), Phys. Rev. D **68**, 114506 (2003).

[8] Y. Aoki *et al.*, Phys. Rev. D **73**, 094507 (2006).

[9] D. J. Antonio *et al.* (RBC Collaboration), Phys. Rev. Lett. **100**, 032001 (2008).

[10] Y. Aoki *et al.*, Phys. Rev. D **72**, 114505 (2005).

[11] Y. Aoki *et al.*, arXiv:0712.1061.

[12] Z. Fodor, S. D. Katz, and K. K. Szabo, J. High Energy Phys. 08 (2004) 003.

[13] H. Fukaya, S. Hashimoto, K. I. Ishikawa, T. Kaneko, H. Matsufuru, T. Onogi, and N. Yamada (JLQCD Collaboration), Phys. Rev. D **74**, 094505 (2006).

[14] S. Aoki, H. Fukaya, S. Hashimoto, and T. Onogi, Phys. Rev. D **76**, 054508 (2007).

[15] J. Noaki *et al.* (JLQCD Collaboration), Proc. Sci., LAT2007 (2007) 126 [arXiv:0710.0929].

[16] T. Kaneko, H. Fukaya, S. Hashimoto, H. Matsufuru, J. Noaki, T. Onogi, and N. Yamada (JLQCD collaboration), Proc. Sci., LAT2007 (2007) 148 [arXiv:0710.2390].

[17] E. Shintani, H. Fukaya, S. Hashimoto, H. Matsufuru, J. Noaki, T. Onogi, and N. Yamada (JLQCD Collaboration), Proc. Sci., LAT2007 (2007) 134 [arXiv:0710.0691].

[18] S. Aoki *et al.* (JLQCD Collaboration), arXiv:0710.1130.

[19] H. Fukaya *et al.* (JLQCD Collaboration), Phys. Rev. Lett. **98**, 172001 (2007).

[20] H. Fukaya *et al.*, Phys. Rev. D **76**, 054503 (2007).

[21] H. Fukaya *et al.* (JLQCD collaboration), Proc. Sci., LAT2007 (2007) 073 [arXiv:0710.3468].

[22] H. Fukaya *et al.* (JLQCD collaboration), arXiv:0711.4965.

[23] H. Matsufuru (JLQCD Collaboration), Proc. Sci., LAT2007 (2007) 018 [arXiv:0710.4225].

[24] S. Hashimoto *et al.* (JLQCD collaboration), Proc. Sci., LAT2007 (2007) 101 [arXiv:0710.2730].

[25] H. Neuberger, Phys. Lett. B **417**, 141 (1998).

[26] H. Neuberger, Phys. Lett. B **427**, 353 (1998).

[27] R. Sommer, Nucl. Phys. **B411**, 839 (1994).

[28] T. Kaneko *et al.* (JLQCD Collaboration), Proc. Sci., LAT2006 (2006) 054 [arXiv:hep-lat/0610036]; S. Aoki *et al.* (JLQCD Collaboration), arXiv:0803.3197.

[29] T. A. DeGrand and S. Schaefer, Comput. Phys. Commun. **159**, 185 (2004); L. Giusti, P. Hernandez, M. Laine, P. Weisz, and H. Wittig, J. High Energy Phys. 04 (2004) 013.

[30] T. Yagi, M. Ohtani, O. Morimatsu, and S. Hashimoto, Proc. Sci., LAT2007 (2007), 086.

[31] G. Martinelli, C. Pittori, C. T. Sachrajda, M. Testa, and A. Vladikas, Nucl. Phys. **B445**, 81 (1995); A. Donini, V. Gimenez, G. Martinelli, M. Talevi, and A. Vladikas, Eur. Phys. J. C **10**, 121 (1999).

[32] M. Ciuchini, E. Franco, V. Lubicz, G. Martinelli, I. Scimemi, and L. Silvestrini, Nucl. Phys. **B523**, 501 (1998).

[33] M. Della Morte, R. Frezzotti, J. Heitger, J. Rolf, R. Sommer, and U. Wolff (ALPHA Collaboration), Nucl. Phys. **B713**, 378 (2005).

[34] D. Becirevic and G. Villadoro, Phys. Rev. D **69**, 054010 (2004).

[35] G. Colangelo, S. Durr, and C. Haefeli, Nucl. Phys. **B721**, 136 (2005).

[36] M. F. L. Golterman and K. C. L. Leung, Phys. Rev. D **57**, 5703 (1998).

[37] R. Brower, S. Chandrasekharan, J. W. Negele, and U. J. Wiese, Phys. Lett. B **560**, 64 (2003).

[38] R. Babich, N. Garron, C. Hoelbling, J. Howard, L. Lellouch, and C. Rebbi, Phys. Rev. D **74**, 073009 (2006).